



Multicomponent Cu-Mn-Fe silica supported catalysts to stimulate photo-Fenton-like water treatment under sunlight

Andraž Šuligoj^{a,b,1}, Ivalina Trendafilova^{a,c,1}, Ksenija Maver^a, Albin Pintar^a, Alenka Ristić^a, Goran Dražić^a, Wael H.M. Abdelraheem^{d,e}, Zvonko Jagličić^f, Iztok Arčon^{g,h}, Nataša Zabukovec Logar^{a,g}, Dionysios D. Dionysiou^d, Nataša Novak Tušar^{a,g,*}

^a National Institute of Chemistry, Hajdrihova 19, SI-1001 Ljubljana, Slovenia

^b Faculty of Chemistry and Chemical Technology, University of Ljubljana, Večna pot 113, SI-1000 Ljubljana, Slovenia

^c Institute of Organic Chemistry with Centre of Phytochemistry, Bulgarian Academy of Sciences, BG-1000 Sofia, Bulgaria

^d Environmental Engineering and Science Program, Department of Chemical and Environmental Engineering, University of Cincinnati, Cincinnati, OH 45221, USA

^e Chemistry Department, Faculty of Science, Sohag University, Sohag 82524, Egypt

^f Institute of Mathematics, Physics and Mechanics & Faculty of Civil and Geodetic Engineering, University of Ljubljana, SI-1001 Ljubljana, Slovenia

^g University of Nova Gorica, SI-5000 Nova Gorica, Slovenia

^h Jožef Stefan Institute, Jamova cesta 39, SI-1000 Ljubljana, Slovenia

ARTICLE INFO

Editor: Despo Fatta-Kassinos

Keywords:

Magnetic catalyst
Photocatalyst
Water treatment
Sunlight
Contaminants of emerging concern
Photo-Fenton-like systems

ABSTRACT

Removal of contaminants of emerging concern (CEC) from water is a serious problem. Using sunlight to assist in this process is one of the most sustainable methods for water treatment. In this study, we demonstrate that tailoring the morphology and optimizing the metal concentration in the multicomponent catalysts through an appropriate synthetic strategy leads to Fenton-like and photo-Fenton-like systems capable of effectively degrading bisphenol A and coumarin as model endocrine disruptors and coumarin as a probe for [•]OH detection. Multicomponent Cu-Mn-Fe silica supported catalysts were prepared via direct synthesis by incorporating magnetic Fe₃O₄ nanoparticles, Mn and Cu during the formation of silica nanoparticles with interparticle mesoporosity. Comprehensive characterization by advanced microscopic and spectroscopic techniques revealed qualitatively and quantitatively the presence of magnetic Fe oxides covered with the silica support, isolated Mn cations/oxo species into silica framework and CuO particles attached to the silica framework. The Fenton-like activities of the catalysts are due to the catalytic disproportionation of H₂O₂ by Cu²⁺ species and isolated Mn species in the silica support. The investigated catalysts are efficient concerning the homolytic cleavage of H₂O₂ to hydroxyl radicals, with a further positive effect of hydroxyl radical formation observed under visible-light illumination thus acting as photo-Fenton-like catalysts. Fe oxides with magnetic properties are used for easy separation of the catalyst/photocatalyst after the reaction and do not contribute to the catalytic/photocatalytic performance.

1. Introduction

During the last decades, water pollution with organic contaminants of emerging concern (CECs) has become a severe issue [1,2]. Among the various possible treatment approaches, advanced oxidation processes (AOPs) that involve the generation of highly reactive oxygen species capable of decomposing organic pollutants unselectively and efficiently into environmentally friendly products (e.g., H₂O, CO₂, and inorganic minerals) are highly prominent. Fenton reaction [3] in which iron salts

(Fenton reagent) are used as homogeneous catalysts in the presence of hydrogen peroxide (oxidant) is being highly researched due to its efficiency, eco-friendliness, and economic viability. The application of classical Fenton processes (homogeneous catalysis) is limited mainly due to three reasons: (i) the need for narrow acidic working conditions (optimal pH is 2.8–3.5), (ii) the generation of large amounts of iron sludge, and (iii) the post-treatment of effluents with excess iron ions to meet their regulatory levels in water [4–6]. Thus, utilizing Fenton-like reaction at neutral pH, using heterogeneous catalytic systems is

* Corresponding author at: National Institute of Chemistry, Hajdrihova 19, SI-1001 Ljubljana, Slovenia.

E-mail address: natasa.novak.tusar@ki.si (N. Novak Tušar).

¹ First author.

suggested to overcome these limitations. Additionally, photo-Fenton approach can bring the advantage of the photocatalytic reaction as well, by producing $\bullet\text{OH}$ via above-bandgap excitation of certain photocatalysts [3,7,8].

Different Fenton-like catalysts can be used to circumvent problems (i) and (ii), such as transition metals (e.g., Al, Ce, Cr, Co, Mn, and Cu), and polyoxometalates (POMs), which show activity via similar reaction mechanisms, however, at near natural pH values [7,9,10]. Manganese, for instance, shows considerable activity under circumneutral pH [11, 12], but its leaching in the system leaves problem (iii) open. In the last years, our work has been aimed at a better understanding of the synthesis, functionality and catalytic performance of the transition metal oxide nanoparticles supported on mesoporous silicas in oxidation reactions. Namely, mesoporous silicas are promising supports for industrial applications because of their excellent stability and durability, if compared to other supports. Our group recently reported a solution to manganese leaching in the system in which Mn was incorporated into mesoporous silica nanostructures and additional Cu was added, which inhibited Mn dissolution by over 50%. [13] Copper, although having a stabilizing effect and showing Fenton-like activity toward CECs via $\bullet\text{OH}$ generation by framework $\equiv\text{Cu}(\text{I})$ [14,15], did not convey any synergism in photo-Fenton reaction. [13] Last but not least, incorporating magnetic-type iron oxide (e.g., magnetite or γ -phase) into porous silica would allow an easy collection and separation of catalyst for further reuse [16–19].

In this article, trimetallic Cu-Mn-Fe catalysts on silica supports were developed for photo-Fenton-like advanced oxidation process (AOP) wastewater treatment under visible light at neutral pH. They were prepared by direct solvothermal synthesis followed by calcination or extraction-calcination. To confirm and complement the characterization results obtained by advanced microscopic and spectroscopic techniques, we performed Mn, Fe and Cu K-edge XANES (X-ray absorption near edge structure) analysis to quantify the valence state and local symmetry of all three metal sites. The catalysts were screened for Fenton-like and photo-Fenton-like degradation of bisphenol A and coumarin as model endocrine disruptors and coumarin as a probe for $\bullet\text{OH}$ detection.

2. Experimental

2.1. Preparation of catalysts

Magnetic iron oxide nanoparticles were synthesized by coprecipitation procedure of iron salts in the presence of a strong base. [20] Thus, Fe_3O_4 was prepared by mixing 0.01 mol $\text{FeCl}_2 \cdot 4 \text{H}_2\text{O}$ and 0.02 mol $\text{FeCl}_3 \cdot 6 \text{H}_2\text{O}$ in a 250 mL three-neck flask, i.e., the final volume is 100 mL solution. Then, a 100 mL of NaOH solution (0.8 M) was added to the iron salt solution in a dropwise manner until a final pH of 12 was attained. The reaction mixture was then stirred at 500 rpm for 3 h under N_2 flow. The obtained solid product was isolated by centrifugation, washed with ultrapure grade water until chloride-free washout is attained. Finally, the precipitate was dried at room temperature and stored in amber vials.

The prepared magnetic iron oxide nanoparticles (25 mg) were dispersed in 25 g silica source (TEOS Aldrich, 98%, Fe/Si=0.01) by ultrasonication for 30 min, then manganese acetate tetrahydrate (Mn $(\text{CH}_3\text{COO})_2 \cdot 4 \text{H}_2\text{O}$, Fluka) and copper acetate monohydrate (Cu $(\text{CH}_3\text{COO})_2 \cdot \text{H}_2\text{O}$, Aldrich) with theoretical molar ratios of Mn/Si and Cu/Si = 0.01 were added to the previous solution and stirred for 10 min. Triethanolamine (8.86 g, 99%, Sigma Aldrich) as a structure directing agent (directs the polycondensation of silicate species) and distilled water (16.4 g) were then added to the mixture under continuous stirring at room temperature. After 30 min, tetraethylammonium hydroxide (8.66 g, 20%, Acros) was added as a pH moderator. The formed gel was aged overnight at room temperature and then dried in a furnace for 24 h at 50 °C. The obtained product was solvothermally treated in a Teflon-lined stainless-steel autoclave (50 mL) at 150 °C for 48 h in ethanol.

The solid product was separated by decantation and washed with ethanol, water and finally dried at ambient room temperature overnight. The pores are freed from the organic compounds (structure directing agent triethanolamine and pH moderator tetraethylammonium hydroxide) via two different procedures: 1) extraction-calcination: extraction with ethanol at 80 °C overnight, followed by calcination at 450 °C for 6 h using a ramp rate of 1 °C/min under continuous flow of air, and 2) calcination: direct calcination at 450 °C for 6 h using a ramp rate of 1 °C/min under continuous air flow. The synthesized materials were denoted as CuMnFeMS-ExC (extraction-calcination procedure) and CuMnFeMS-C (calcination-only procedure), where MS stands for mesoporous silica.

2.2. Characterization

X-ray powder diffraction (XRD) was used to investigate the structural characteristics of the new materials. The diffractograms were recorded on a PANalytical X'Pert PRO high-resolution diffractometer using Cu $K\alpha 1$ radiation ($\lambda = 0.15406 \text{ nm}$) with an accelerating voltage of 40 kV, and an emission current of 30 mA.

Textural properties of the obtained catalysts were studied by nitrogen physisorption isotherms measured on a Micromeritics Tristar 3020 apparatus recording at $-196 \text{ }^\circ\text{C}$. The samples were outgassed at 200 °C for 2 h. The BET-specific surface area was calculated from adsorption data in the relative pressure range from 0.06 to 0.165. [21] The total pore volume was estimated based on the amount adsorbed at a relative pressure of 0.98. [22] The pore size distributions (PSDs) were calculated from nitrogen adsorption data using an algorithm by Barrett, Joyner, and Halenda (BJH) method. [23] The mesopore diameters were determined as the maxima on the PSD for given samples. The surface morphologies of samples were examined by Zeiss Supra™ 35VP (Carl Zeiss) field-emission scanning electron microscope (FE-SEM) operating at 1 kV and using a 10 μm aperture. The elemental compositions of the surface of the catalysts were studied by energy dispersive X-ray analysis (EDX) with an INCA Energy system attached to the microscope.

The surface charge of the materials was measured in the pH range of 1–12 by Zetasizer nano ZS instrument (Malvern) using electrophoretic light scattering technology. To adjust the pH, 0.1 M NaOH or 0.1 M HCl were used.

High-Resolution Scanning Transmission Electron Microscopy (HR-STEM) was used to investigate the morphology, particle size of the obtained materials and the presence of iron, copper, and manganese, and oxide clusters in the silica matrix. The analysis was performed on Cs probe corrected scanning transmission electron microscope ARM 200 CF (JEOL) with the cold-FEG cathode. The microscope was equipped with a dual-EELS system Quantum ER from Gatan and Centurio EDXS system with a 100 mm^2 SDD detector. For HR-STEM studies a drop of sample suspension in ethanol was placed on a lacey-carbon coated nickel grid and dried at room temperature. To minimize the electron beam-induced damage 80 kV accelerating voltage was used for analysis.

Raman spectra were recorded in the spectral range from 100 to 1400 cm^{-1} using a Witec Alpha 300 confocal microscope that employed a green laser with an excitation wavelength of 532 nm, an accumulation time of 50 s, and a resolution of 4 cm^{-1} . For each sample, three different locations were analyzed to verify the spectra.

UV–VIS diffuse reflectance absorption spectra of powders were recorded on a Lambda 650 (Perkin Elmer) UV–VIS spectrophotometer, equipped with a Harrick Praying Mantis accessory at the scan speed 266 nm/min , and the slit width set to 3 nm. Spectralon® was used for background correction.

Residual and leached metals (i.e., Cu, Mn, and Fe) were monitored in the degradation system by inductively coupled plasma-optical emission spectrometry (ICP-OES, model 715-ES, Varian).

Cu, Mn, and Fe K-edge X-ray absorption spectra (XAS) were collected at BM23 beamline at the European synchrotron radiation facility (ESRF, Grenoble, France). The measurements were performed in transmission

mode using ionization chambers as detectors. For Cu K-edge measurements, the first chamber was filled with 300 mbar Ar, whereas the second and third chambers were filled with 1400 mbar pure N₂ to obtain 15% and 70% absorption at 9.0 keV in the first and in both the second and the third chamber, respectively. For the Fe and Mn K-edge measurements, the first chamber was filled with 220 mbar Ar, and the second and the third chambers were filled with 50% N₂/He mixture, with total pressure being 2.0 bar. A Si(111) double-crystal monochromator with energy resolution of 1 eV at 9 keV was used for energy scanning. Flat Si mirrors positioned at a grazing angle of 3 mrad were employed for harmonic rejection. The sample catalysts and reference compounds were prepared as homogeneous self-supporting pellets with a total absorption thickness (μ d) of about 2.5 above the corresponding K-edges. The absorption spectra of the samples were measured within the interval [-150 eV, 1000 eV] relative to the K-edges. In the XANES region equidistant energy steps of 0.2 eV were used, while in the EXAFS region equidistant k -steps ($k = 0.035 \text{ \AA}^{-1}$) were adopted. The integration time was set to 2 s/step. Two or three scans of each spectrum were collected to improve signal-to-noise ratio. Exact energy calibration was established with the simultaneous absorption measurements on corresponding metal (Cu, Mn, Fe) foil inserted between the second and third ionization cell. The analysis of XANES spectra was performed with the Athena (Demeter) program package [24].

The magnetization was measured with a Quantum Design MPMS-XL-5 SQUID magnetometer.

2.3. Catalytic and photocatalytic removal of bisphenol A (BPA) and coumarin

The tests were conducted in a cylindrical 100 mL double-walled glass reactor (height 30 mm, diameter 60 mm). The temperature was regulated to 25 °C (F25/ME, Julabo). 100 mL of BPA solution (10 mg/L) was introduced into the reactor and 40 mg of catalyst was added and mixed for 60 min to establish adsorption-desorption equilibrium. Then, H₂O₂ (final concentration 20 mM, or varied in some reactions) was added and, in the case of photocatalytic tests, an LED lamp (KL 2500 LED, Schott) was switched on. Samples (1 mL) were taken at desired time intervals and 500 μ L of methanol was added to scavenge the remaining peroxide. The samples were immediately centrifuged (6000 rpm, 3 min) to remove the solid particles. Samples were analyzed by a HPLC instrument (Shimadzu) using a C-18 column (Phenomenex) in isocratic mode with 30% methanol and 70% water, at a flow rate of 0.7 mL/min. In cases where pH was controlled, the acidity was monitored with 827 pH lab instrument (Metrohm) and actively controlled within ± 0.1 pH units by using 0.01 M HCl. The continuous catalytic tests were performed in the same manner, only decreasing the initial concentration of BPA to 5 mg/L, and upon reaching its total degradation, spiking the reaction mixture again with BPA to regain its initial concentration.

The formation of hydroxyl radicals in the presence of investigated solids was measured by using photoluminescence method with coumarin (COUM, 98%, p.a., Alfa Aesar, USA) as a probe compound. The measurements were conducted in a glass double-wall batch slurry reactor (Lenz Laborglas). A photocatalyst (20 mg) was suspended in 100 mL of an aqueous solution containing 1.4 mM COUM that was thermostated (F25/ME, Julabo) at $T = 25 \text{ }^\circ\text{C}$. The suspension was stirred (400 rpm) in the dark for 20 min before the addition of 30% H₂O₂ ($c_0 = 20 \text{ mM}$) and illumination with a visible lamp (KL 2500 LED, SCHOTT). Aqueous-phase samples were withdrawn during the illumination period in different time intervals and immediately filtered through a 0.2 μ m membrane filter (regenerated cellulose). The samples were then analyzed by recording the photoluminescence signal of the generated 7-hydroxycoumarin using a UV/Vis photoluminescence spectrometer (LS 55, Perkin Elmer). The scanning speed was 200 nm/min, and the wavelength of the excitation light was set to 315 nm. The excitation and the emission slits in the instrument were both set to the width of 5 nm.

3. Results and discussion

3.1. Physicochemical characterization

Catalysts were first examined with solid state characterization techniques to elucidate their morphology, structure and optoelectronic properties. XRD reflections of the obtained catalysts (Fig. 1) indicate the obtained materials were in the nanosize range. Iron-oxide particle size calculated by the Scherrer equation applying the profile fitting method was 10 nm, which was consistent with previously reported results for iron-oxide nanoparticles prepared by the same procedure [20,25]. Superparamagnetic magnetite (Fe₃O₄) nanoparticles were reported to oxidize into maghemite (γ -Fe₂O₃) and possibly into superparamagnetic material with considerable saturation magnetization when exposed to air and humidity [25]. Maghemite was previously observed to form as a shell layer on the surface of magnetite nanoparticles of the same size and resulted in the stabilization of the core particles against further oxidation [26]. Magnetite and maghemite cannot be distinguished by X-ray diffraction due to the overlapping of widened reflections typical of small nanoparticles (see Fig. 1 and references for magnetite and maghemite). The XRD pattern of the CuMnFeMS-C material confirmed the amorphous, mesoporous structure of silica and shows the presence of nano-sized magnetite and/or maghemite with the low intensity of their corresponding peak (due to the low content of iron oxides particles in the catalysts). The pattern of CuMnFeMS-C catalyst contains typical reflections for CuO particles with 25 nm size as calculated by the Scherrer equation, but no reflections for MnO_x. The template removal procedure of extraction-calcination affected the structure of the prepared CuMnFeMS-ExC and diffraction peaks with low intensity are observed only for iron oxides. This means that both, CuO and MnO_x nanoparticles, are too small (< 5 nm) to be detected by XRD, however, they were detected by other characterization techniques (TEM, Raman, XANES, see discussion below). The difference in the size of the oxide particles for both samples could be explained by sintering of the not-well-attached metal species during the high temperature calcination for CuMnFeMS-C, while for sample CuMnFeMS-ExC these species are already removed during the extraction procedure, and formation of bigger crystallites is less probable.

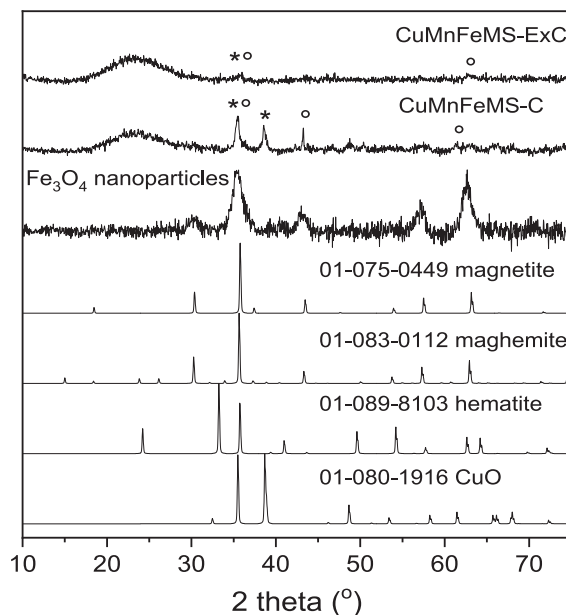


Fig. 1. XRD patterns of synthesized Fe₃O₄ nanoparticles, CuMnFeMS-C, CuMnFeMS-ExC and reference patterns of CuO, hematite (α -Fe₂O₃), maghemite (γ -Fe₂O₃) and magnetite (Fe₃O₄). The marked reflections in samples denote the CuO (*) and Fe₃O₄ (o) phases.

The additional extraction procedure aids to remove the not-well-attached particles of metal species from the silica support. Although SEM imaging (Fig. S1) did not convey clear differences in morphologies among the samples and they both show formation of porous structure with interparticle porosity, the elemental composition, derived from the EDXS analysis of powders (Table 1), shows a decrease in metal content upon extraction procedure only for copper.

Uniform amorphous, mesoporous structures of the catalysts are seen in TEM images (Fig. 2) with the presence of oxide nanoparticles of the catalysts as observed from the dark spots. EDXS mapping (Figs. S2–S4, Supporting information) has confirmed the existence of CuO and Fe_xO_y nanoparticles in both samples. Moreover, Fe, Cu, and Mn were uniformly distributed at the atomic scale inside the silica matrix of the catalysts. However, the designation of iron oxide to a particular phase was not possible.

We were, however, able to assess the “average” valence state of iron via quantification of Fe L_{2,3}-edge in EELS spectrum. This method determines the valence state of Fe (and consequently the stoichiometry of iron oxide). For sample CuMnFeMS-C (Fig. 3g) the ratio of Fe L₃/L₂ lines equals to 4.3. If compared to our previous study [28] we can conclude that the “average” valence state of Fe in those nanoparticles is around 2.8 indicating the mixture of Fe₃O₄ and Fe₂O₃.

Further investigation of the oxide components in the samples was conducted using Raman spectroscopy (Fig. 3a). A relatively broad range of bands was covered by the spectra; therefore, overlapping bands made it difficult to resolve between them. Off note, pure iron oxide nanoparticles were prepared separately for comparison purposes. Consistently with XRD and TEM results, the Raman spectrum of iron oxide nanoparticles revealed three broad bands in the regions 250–430 cm⁻¹, 430–560 cm⁻¹, and 560–800 cm⁻¹, corresponding to magnetite (Fe₃O₄) and maghemite (γ-Fe₂O₃) phases of iron oxide. Magnetite was previously shown to exhibit strong bands at 680 and 293 cm⁻¹, broad bands at 447–470 cm⁻¹, and weak bands at 580 and 324 cm⁻¹ [29–32]. In the current study, the three bands at 355, 497, and 710 cm⁻¹ agreed with those reported for maghemite [30,33]. Additionally, the band observed at 378 cm⁻¹ and the shoulder peak above 710 cm⁻¹ were explained by the transformation of magnetite into maghemite due to either heating of the sample by laser light during the measurements or due to sample exposure to air after the preparation. Fe₃O₄ nanoparticles are well reported to be relatively unstable and sensitive to oxidation [34].

The Raman spectrum of the CuMnFeMS-C sample reveals the presence of different crystalline phases, i.e., hematite, magnetite, and maghemite. Hematite was obtained during calcination at 450 °C.[35] The iron oxide α-Fe₂O₃ exhibits bands at 293, 410, 497 and 618 cm⁻¹ [32]. The intense band at 293 cm⁻¹ can be attributed to CuO as well as to magnetite (Fe₃O₄). The bands at 818, 490, and 410 cm⁻¹ belonged to the symmetric Si–O–Si stretching mode, 4- and 5- or 6-member siloxane rings, respectively [36]. Additionally, several bands (293, 342, and 618 cm⁻¹) can be attributed to CuO [37] nanoparticles as well as shoulders (324, 380, 580, and 650 cm⁻¹) dedicated to manganese oxides nanoparticles [38]. The intense bands centered at 293 and 620 cm⁻¹ indicates the presence of large nanoparticles of CuO in the CuMnFeMS-C sample.

The Raman spectrum of the CuMnFeMS-ExC catalyst encompasses bands at 812, 611, 501, and 411 cm⁻¹ corresponding to Si–O–Si siloxane bridges and 3-, 4-, 5- or 6- member siloxane rings, respectively. The bands at 687, 532, 470, and 447 cm⁻¹ were assigned to magnetite, while bands centered at 710, 501 and 360 cm⁻¹ are dedicated to γ-Fe₂O₃

Table 1
Elemental composition and molar ratios of the obtained samples from SEM EDX analysis.

Catalyst	Mn/Si	Cu/Si	Fe/Si
CuMnFeMS-ExC	0.005	0.01	0.03
CuMnFeMS-C	0.005	0.02	0.03

(maghemite). The presence of hematite (α-Fe₂O₃) in the catalyst was evident by the observed bands at 611, 411, 501, and 290 cm⁻¹. In addition, the bands observed at 266, 316, 360, 562, and 666 cm⁻¹ show the presence of the nanoparticles of manganese oxides (Mn₃O₄ and Mn₂O₃), which are not detected by XRD. In agreement with EDX results, only shoulders (620, 340, and 290 cm⁻¹) of CuO can be observed due to the smaller size of these nanoparticles in the catalyst [37].

UV–VIS absorption properties of the materials are shown in Fig. 3b–c. Panel (b) presents catalysts prepared via the two procedures that involve single metals for better understanding of the light response of single metal-incorporated catalysts, especially in the > 400 nm range where the photo-Fenton-like tests were conducted (see below). In single metal samples, the highest absorption in 400–800 nm range was observed with CuMS-C and MnMS-ExC samples. We note that in CuMS-ExC sample absorption was low in the 400–800 nm range but exhibited a hump ~750 nm, assigned to the d–d transition of Cu²⁺ in the distorted octahedral field of oxygen ligands [13], hence still showing the presence of these species. The high energy part of the plot (200–300 nm) can be assigned to M–O charge-transfer (CT) of the isolated metal centers of Mn³⁺, Fe³⁺ and Cu²⁺ ions [39–41]. For iron, in general, d–d transitions of Fe³⁺ are expected between 350 and 550 nm, and are weak since they are symmetry and spin forbidden [41]. These can clearly be seen in both Fe samples; FeMS-ExC and FeMS-C, while isolated Fe³⁺ species at 230 nm are visible only in FeMS-ExC. The data here are consistent with Raman results showing iron environment typical for magnetite (Fe₃O₄) and maghemite (γ-Fe₂O₃) phases. For copper, the data suggest on the presence of a mixture of different-sized CuO particles on the surface of Cu-modified catalysts, by the appearance of band at ~240 nm (Cu²⁺ ← O²⁻ transitions) and the absorption at 620–800 nm (d–d transitions of Cu²⁺ in the distorted octahedral field of oxygen ligands) [13]. The latter transition is greatly reduced upon extraction procedure, suggesting lower number or smaller of CuO NPs, which agrees with Raman, TEM and XRD data. As regards manganese, these spectra are also complex indicating on manganese present in multiple coordination environments. The broad band between at 400–540 nm can be assigned to the presence of different octahedrally coordinated Mn³⁺ and Mn²⁺ in manganese oxides, respectively [42]. The band centered at 260 nm is commonly referred to the framework tetrahedrally coordinated Mn³⁺ [43]. The intensity of both bands is reduced in sample with extraction procedure (Fig. 3b).

The spectra with all three metals (Fig. 3c) show highly complex picture. It should be noted that features assigned in single metal samples above do not necessarily hold for the multi-metal sample. Upon adding the extraction procedure to multi-metal sample there appears an increase in high energy band at ~255 nm and a concurrent decrease in absorbance of wavelengths longer than 300 nm. The increase originates from the rise in absorbance from isolated metal species (see discussion above) while the decrease stems from lower amounts of larger CuO particles and lower portion of manganese oxides [13]. This corroborates the results from Raman which suggested on decreased amount of Cu- and Mn-oxides in the extracted sample.

Specific surface area, total pore volume, and average pore sizes of CuMnFeMS-ExC and CuMnFeMS-C catalysts were estimated from adsorption–desorption isotherms (Fig. 3d–e) and the results are summarized in Table 2. Both samples show sorption isotherms typical for silica with interparticle mesoporosity [12] with a relatively narrow type IV isotherms. The hysteresis loop resembles an H3 type, hinting on interparticle porosity in non-rigid aggregates. The samples show a bit of deviation from our previous results, where the extraction procedure increased the specific surface area (~30%) and decreased the average pore size (~15%) [44]. The reasons might lie in the presence of an iron oxide core, which could stabilize the surrounding silica pore structure during the extraction procedure. The elucidation of exact reasons for this difference is still unknown and beyond the scope of this report.

Measurements of surface charge according to pH (Fig. 4) show that at a nearly neutral pH (6–7), both catalysts exhibit a negatively charged

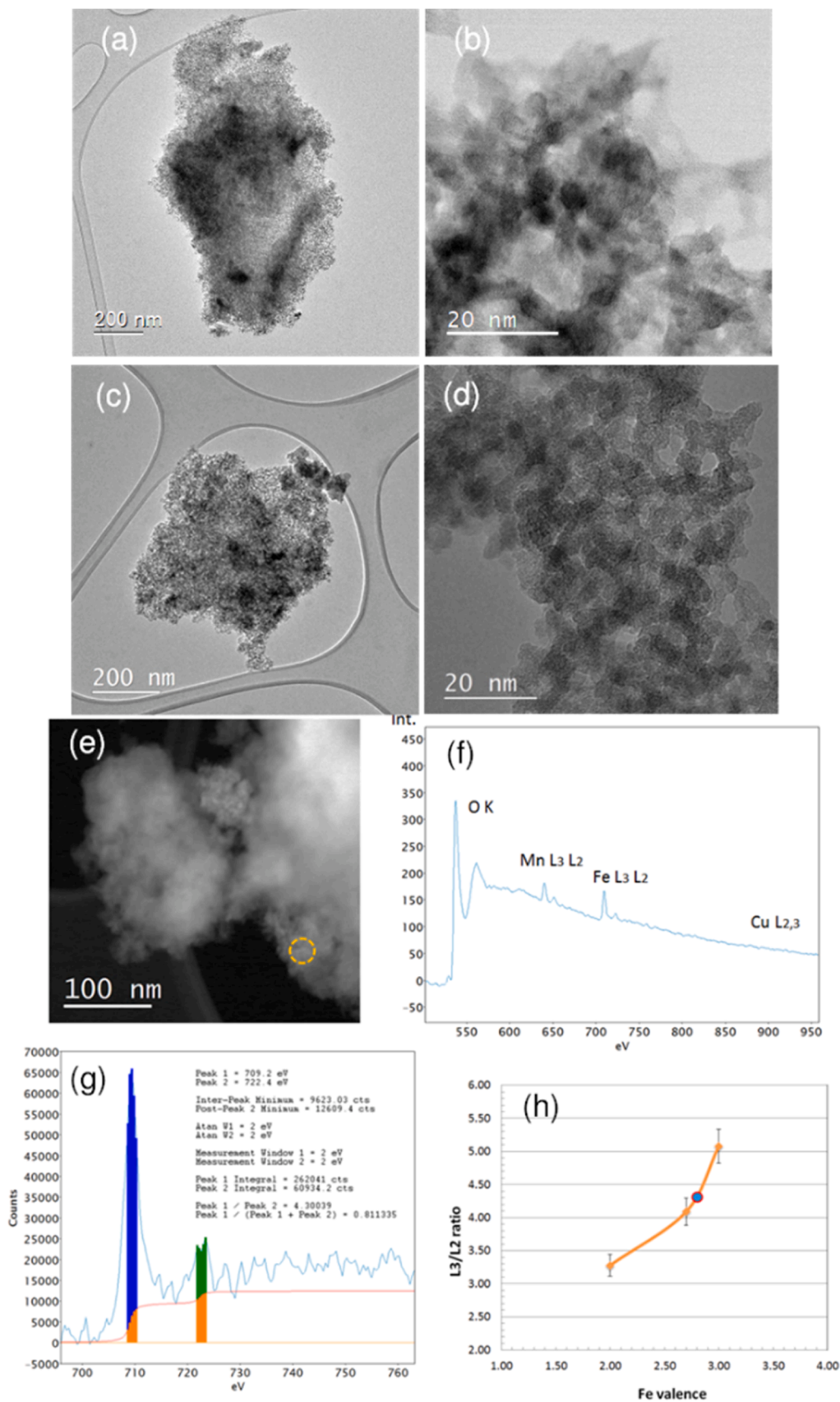


Fig. 2. TEM micrographs of CuMnFeMS-ExC (a, b) and CuMnFeMS-C (c, d) samples with uniform mesoporous amorphous structure with visible darker areas, (e) HAADF-STEM image of CuMnFeMS-C sample, and (f) EELS spectrum from labelled area in (e). Facet (g) shows determination of Fe valence state from L3/L2 lines ratio using double arctangent method, and (h) depicts the calibration curve from our previous work [27].

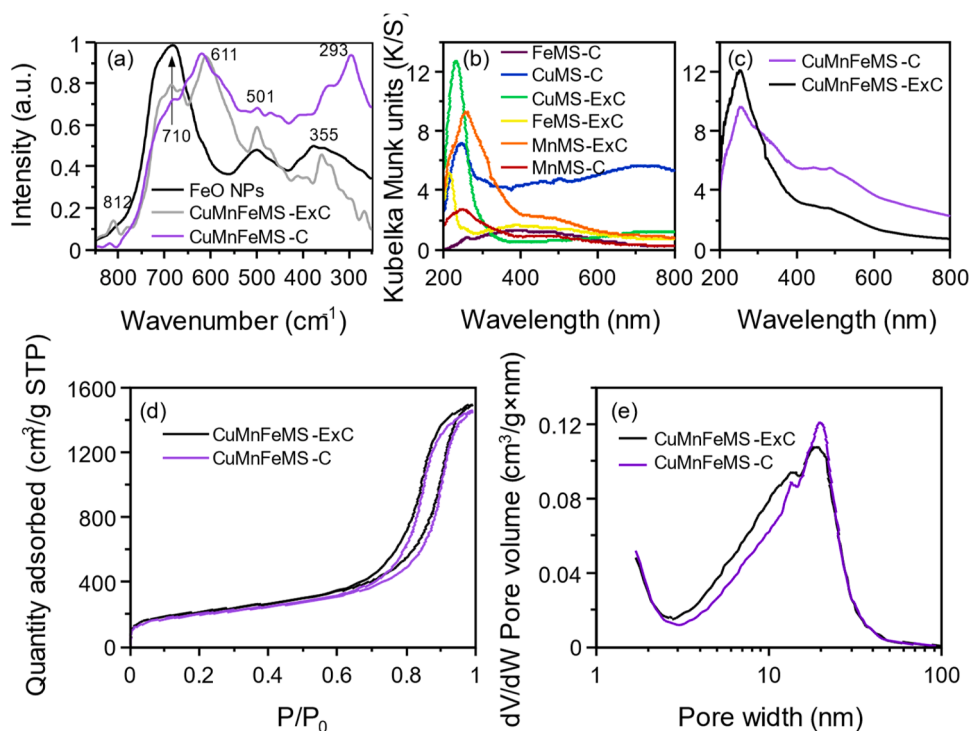


Fig. 3. Spectroscopic analyses of samples. Raman spectra of iron oxide nanoparticles, and samples CuMnFeMS-C and CuMnFeMS-ExC (a), UV-VIS diffuse reflectance absorption spectra of powders of single metal (b) and tri-metal catalysts (c). Nitrogen sorption isotherms (d) and the derived adsorption pore size distributions using according to BJH algorithm (e).

Table 2

Textural properties of the obtained catalysts.

	CuMnFeMS-ExC	CuMnFeMS-C
S_{BET} (m ² /g)	731	781
V_p at $P/P_0 = 0.98$ (cm ³ /g)	2.227	2.287
Average pore size (nm)	13.5, 19.6	13.8, 19.3

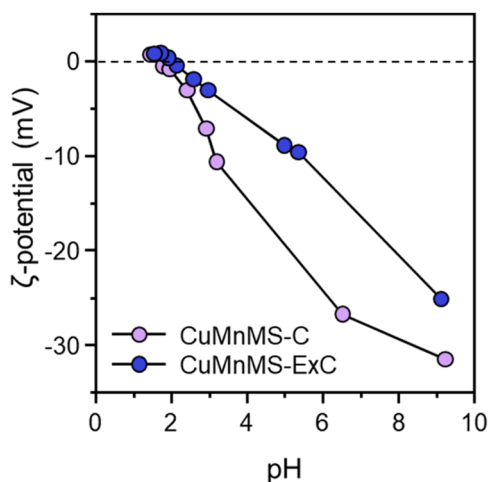


Fig. 4. Zeta potential versus pH showing the position of the isoelectric point (dashed line) for the two catalysts.

surface, i.e., -25 mV for CuMnFeMS-C and -15 mV for CuMnFeMS-ExC. The catalysts exhibit acidic surface with IEP of 3.2 showing a typical quasi-sigmoidal curve. A slight basic shift can be seen in the sample prepared by extraction. One should not ignore the influence of the potential dissolution of the metal ions in the suspension, as this

increases the zeta potential of the suspension [45]. However, the measured leached amounts of metal ions were too low for such an effect (see below, Table 4) and were lower in the sample prepared by extraction, so this reasoning can be ruled out.

Cu, Mn, and Fe K-edge XANES (X-ray absorption near edge structure) analysis was used to determine valence states and local symmetries of the metal cations in the CuMnFeMS-ExC and CuMnFeMS-C catalysts. The relative amounts of metal cations with different valence and local symmetry can be determined by the linear combination fit (LCF) [24] of the XANES spectra with XANES spectra of adequate reference compounds. A more detailed description of the method can be found in the Supplementary information file.

The LCF analysis of the Cu K-edge XANES spectra of CuMnFeMS-ExC and CuMnFeMS-C (Fig. S6 in Supporting information), shows that all the Cu cations are in divalent form. A mixture of nano and micro size CuO particles is identified. The spectrum of CuMnFeMS-ExC is identical to the XANES spectrum of the reference CuO nanoparticles with 2 nm diameter. The spectrum of the calcined catalyst (CuMnFeMS-C) can be completely described by a linear combination of two reference XANES spectra: 52% of the 10 nm CuO nanoparticles, and 48% of the crystalline CuO [46]. LCF results are listed in Table 3 and the quality of the fits are

Table 3

Relative amount (%) obtained by LCF of reference XANES profiles in the CuMnFeMS-ExC and CuMnFeMS-C samples. Uncertainties in relative amounts are given in parentheses.

Cu K-edge	Crystal CuO	10 nm CuO	2 nm CuO
CuMnFeMS-ExC	0	0	100
CuMnFeMS-C	48(1)	52(1)	0
Mn K-edge	01MnKIL	Mn ₂ O ₃	
CuMnFeMS-ExC	92(1)	8(1)	
CuMnFeMS-C	80(1)	20(1)	
Fe K-edge	Fe ₃ O ₄	γ-Fe ₂ O ₃	FePO ₄
CuMnFeMS-ExC	0	72(2)	28(2)
CuMnFeMS-C	6(8)	56(8)	38(3)

shown in Fig. S5 in the Supporting information. The Cu K-edge XANES results are consistent with the results from XRD and TEM, where larger CuO particles were observed in the case of the calcined catalyst.

The LCF analysis of Mn K-edge XANES spectra of the CuMnFeMS-ExC and CuMnFeMS-C catalysts show that the average oxidation state of Mn is between 2+ and 3+ (Fig. S8, Supporting information). Both spectra can be described by a linear combination of the reference sample 01MnKIL, which is used as a reference for manganese cations incorporated into the mesoporous silica framework with Mn/Si = 0.01 and contains Mn²⁺ and Mn³⁺ cations in the ratio of 30%/70% [12], and reference crystalline Mn₂O₃ spectrum. The goodness of linear combination fits is shown in Fig. S8 in the Supporting information. The relative amount of the two reference XANES profiles (01MnKIL and Mn₂O₃) obtained by LCF (Table 3) indicate that the relative amount of Mn³⁺ in both samples is high: 72% in CuMnFeMS-ExC and 76% in CuMnFeMS-C, the rest are Mn²⁺ cations. The obtained molar ratios of Mn²⁺ and Mn³⁺ in the samples are consistent with the Raman and UV-VIS spectroscopy results in this study, as well as with previous studies on the incorporation of Mn cations into porous silicates [12,44]. The high relative ratio of the reference compound 01MnKIL obtained in the LCF fits of the catalyst spectra indicates that in both catalyst samples large majority of Mn cations are incorporated into the silicate framework, which is in good agreement with the EDXS studies, which shows that manganese is homogeneously distributed in the catalysts, and the XRD results, where no diffraction peaks of crystalline Mn-oxides were detected in the catalysts.

The Fe K-edge edge profile of all catalysts are similar (Fig. S9 in Supporting information) and their energy position indicates that the majority of Fe cations are in Fe³⁺ valence state. The pre-edge resonance at 7114 eV in the XANES spectra shows that tetrahedrally coordinated Fe cations are present in the catalysts (Fig. S8 in Supporting information). To analyze the spectra by linear combination fit (LCF), we choose three suitable references to completely describe all XANES profiles:

(i) Fe₃O₄ (magnetite), with Fe²⁺ and Fe³⁺ cations in the inverse spinel structure, in which the Fe²⁺ cations occupy octahedral sites and the Fe³⁺ cations are divided between the octahedral and tetrahedral sites. The ratio of Fe³⁺/Fe²⁺ and the ratio of tetrahedral/octahedral sites is 2:1 [47–49].

(ii) γ-Fe₂O₃, maghemite, which contains only Fe³⁺ cations at octahedral and tetrahedral coordinated sites in the inverse spinel structure, in which the ratio of occupied octahedral to tetrahedral sites is 2:1 [47–49].

(iii) FePO₄ is used as a reference for the tetrahedrally coordinated Fe³⁺ cations [48,49].

The relative amount of each Fe XANES spectrum of reference Fe compounds as determined by LCF analysis is given in Table 3. Examples of LCF analyses are shown in Fig. S10 in Supporting information. From the results obtained by LCF analysis of Fe XANES spectra of both catalyst samples, the relative amount of Fe²⁺/Fe³⁺ ions and relative Fe occupancy of tetrahedral and octahedral sites were determined (Table S3 and S4). The information was used to calculate the unpaired spins that contribute to magnetic properties of the catalysts. A detailed description of the procedure is given in Supplementary information (Table S4 unpaired Fe²⁺ and Fe³⁺). The results based on the Fe K-edge XANES data indicate that the total magnetic moment in calcined tri-metal CuMnFeMS-C is expected to be approximately 3-times larger compared to CuMnFeMS-ExC sample.

Magnetization curves, $M(H)$, of the CuMnFeMS-C, CuMnFeMS-ExC and reference Fe₃O₄ nanoparticles were measured at room temperature between -5 T and 5 T. The results are shown in Fig. S10 in the Supporting information. The curves have a steep increase already in a small magnetic field with no hysteresis, which is typical for materials that can be easily magnetized and attracted by the external magnetic field (a demonstration of the magnetic force of an external magnet acting on catalyst dispersed in a water solution is shown in Fig. S11). The magnetic properties (magnetic moments of a single nanoparticle and saturation magnetization) of the catalysts and reference Fe₃O₄ were

determined by fitting the magnetization curves. The results and a detailed description of the analysis are given in Table S5 in Supplementary information. By comparing the saturation magnetization of the catalysts to the reference Fe₃O₄ nanoparticles, a mass ratio of magnetic nanoparticles was determined. The estimation shows there was 5.6% and 1.9% mass ratio of magnetic nanoparticles in the CuMnFeMS-C and CuMnFeMS-ExC catalysts, respectively. The obtained total magnetic signal was almost 3-times larger in the calcined CuMnFeMS-C compared to CuMnFeMS-ExC, which agrees with the results obtained from XANES.

3.2. Fenton-like and photo-Fenton-like catalytic activity

The catalytic and photocatalytic activities of prepared tri-metallic catalysts were tested for the degradation of bisphenol A via Fenton-like processes. In these Fenton-like tests, batch reactions were employed at an initial BPA concentration of 10 mg/L. A series of experiments were conducted to test the optimal H₂O₂ concentration for the CuMnFeMS-ExC (Fig. 5a). The optimal H₂O₂ concentration was 20 mM, which is consistent with the generally accepted optimal concentration for manganese [10]. This concentration is ~200 × higher than the concentration of manganese in the system (0.12 mM) or Fe (0.106 mM) and about 300 × higher than the concentration of copper (6.215 μM) determined by EDXS analysis (Table 1). The value for the latter is close to that reported by Pachamuthu et al. [50] (H₂O₂: Cu ratio of 300:1), who used Cu-supported/3D mesoporous TUD-1 silica for the degradation of BPA. In the current study, manganese oxide, CuO, and iron oxide nanoparticles with varying physicochemical properties were found to

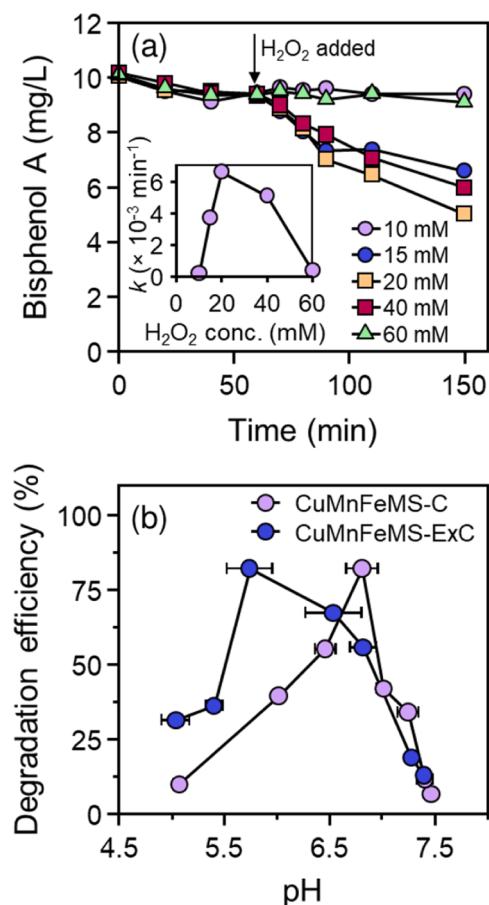


Fig. 5. Optimization of the concentration of H₂O₂ for sample CuMnFeMS-ExC (a) and the degradation efficiencies for the two samples (b). Reaction conditions: $\gamma(\text{cat}) = 400 \text{ mg/L}$, $\gamma(\text{BPA}) = 10 \text{ mg/L}$, in (b) $c(\text{H}_2\text{O}_2) = 20 \text{ mM}$, reaction time = 4 h; the horizontal error bars represent the pH variations during the reaction.

exhibit pH-dependent behavior in the catalysts. Therefore, Fenton-like reactions were performed at different pH values to obtain the optimum conditions for both catalysts.

The degradation efficiencies varied significantly with changing the pH of the reaction system (Fig. 5b). The pH was actively controlled as described in the experimental part. The CuMnFeMS-ExC with smaller CuO nanoparticles sample revealed a maximum (optimum) degradation efficiency of 80% at solution pH 5.7, while BPA degradation by CuMnFeMS-C sample recorded its maximum value of 80% at the optimum pH of 6.7. For all further catalytic tests, these two optimal pH ranges were used for ExC and C sample, respectively.

To confirm the roles of metals in the catalyst, a set of experiments was done where the same catalyst was prepared, only using a single metal incorporated in SiO₂ at a time (Fig. 6a).

In this case, only copper and manganese are responsible for the Fenton-like effect, while iron shows no activity. The effect of Mn and Cu is almost the same, while Mn also shows a higher adsorption capacity for BPA. The lack of activity of Fe is explained by its encapsulation in the core of silica, which separates it from the range of H₂O₂. Interestingly, combination of all three metals produced the highest Fenton like activity (Fig. 6c).

The photo-Fenton reaction showed similar results (Fig. 6b). Again, the two active components were Cu and Mn, while Fe showed no activity even when illuminated with visible light and in the presence of 20 mM H₂O₂. This fact was quite surprising since hematite, maghemite, and magnetite were detected as crystallographic phases in the sample. Iron oxides are good absorbers of visible light (as shown in Fig. 3b–c). However, due to their position inside the Si particle, the charge carriers formed during illumination could not cross the Fe/Si barrier or overcome the subsequent distance of the SiO₂ particle from the surface. On the other hand, the Mn and Cu particles were located both inside the Si network and on the surface of the silica particle, so they could be active in the Fenton-like and photo-Fenton reactions using H₂O₂. The latter also proved to be crucial for the photo-Fenton reaction for both active metals. Copper, for example, showed no activity using only VIS (Fig. 6b), thus requiring H₂O₂ to produce reactive oxygen species. This production was accelerated by the presence of visible-light illumination in the presence of Cu and Mn species on the surface of the silica particle. Similarly, H₂O₂ can be produced in-situ by an appropriate system such as with Zhang et al. [51] Their photo-Fenton system including CdS and g-CN was able to produce similar degradation kinetics of BPA destruction as in this work.

The photo-Fenton-like activity of the tri-metal catalysts concerning BPA removal (Fig. 6c) did not show any synergy with the already enhanced activities of the tri-metal catalysts. Interestingly, the kinetics of the extracted sample is higher here both case when light was applied and when it was not.

The introduction of light induces H₂O₂ dissociation according to equation $\text{H}_2\text{O}_2 + e^- \rightarrow \cdot\text{OH} + \text{OH}^-$ [7], and thus changes the local pH surrounding the Cu site. In this case the electron comes from the illuminated semiconductors (Mn and mostly Cu). To confirm this mechanism, $\cdot\text{OH}$ production was monitored using coumarin as a highly selective $\cdot\text{OH}$ probe [52] (Fig. 7). In the dark, as with BPA degradation, the metal with the highest production of $\cdot\text{OH}$ was copper, followed by manganese, while iron was practically inactive. When visible light was introduced (Fig. 7b), $\cdot\text{OH}$ production was increased substantially. This confirms the formation of additional $\cdot\text{OH}$ during illumination, and, since Cu²⁺ is the main Fenton-like and visible-light active component in our system, the mechanistic aspects of the system will be regarded in terms of Cu²⁺. The following reactions are present in Cu-mediated Fenton-like systems.

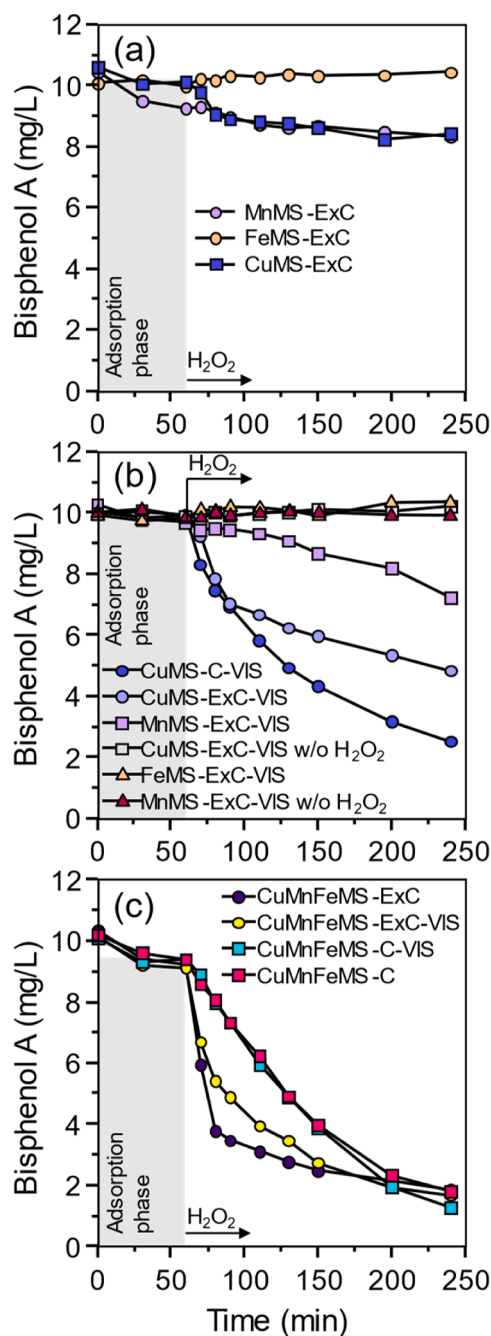
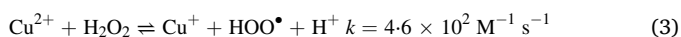
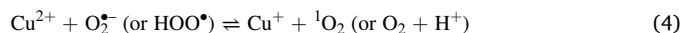


Fig. 6. Fenton-like (a) and photo-Fenton-like (b) degradation of BPA under optimal pH values for the various single-metal samples. In (c) Fenton and photo-Fenton-like reactions of three-metal samples are shown, respectively. Reaction conditions: $\gamma(\text{cat}) = 400 \text{ mg/L}$, $\gamma(\text{BPA}) = 10 \text{ mg/L}$, $c(\text{H}_2\text{O}_2)_0 = 20 \text{ mM}$. Experiments with no H₂O₂ added are marked w/o H₂O₂.



As the reaction medium contains $[\text{H}_2\text{O}_2] \gg [\text{HO}^\bullet]$ and $[\text{O}_2^{\cdot-}]$ these radicals may react with additional peroxide to form other species.



These are slow compared to the Cu-catalyzed reactions, but serve to prevent accumulation of one radical over the other during reaction initiation, or as radicals are scavenged outside of the catalytic cycle.

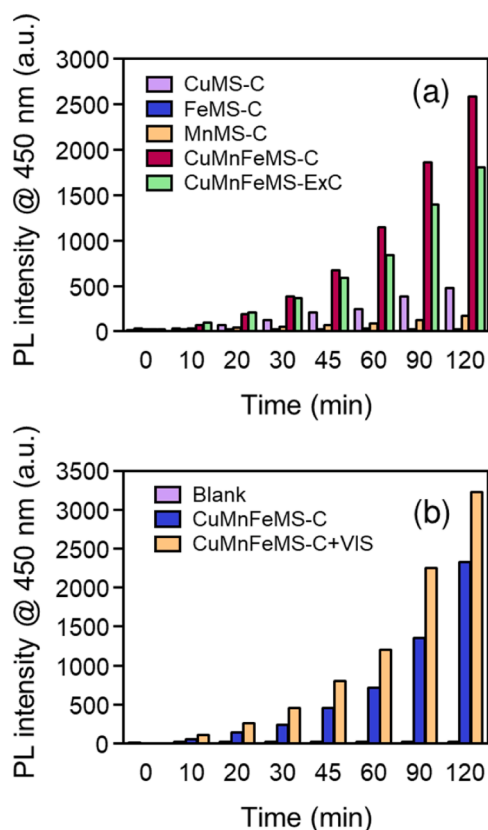
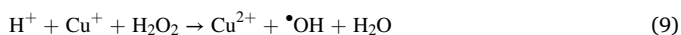
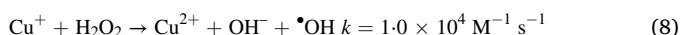
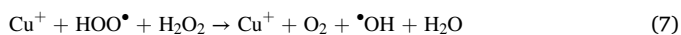


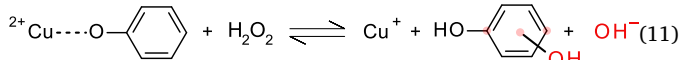
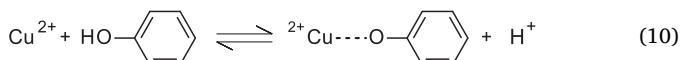
Fig. 7. Levels of 7-hydroxycoumarin as measured by the PL intensity through time in the dark conditions (a) and during visible light irradiation (b).

Hence, the overall kinetics depends on the rate of the Cu^{2+} reduction to Cu^+ , (Eq. 3). This equation is accelerated under high pH which explains the observed pH dependence (Fig. 5b).

The $\text{Cu}^{2+}/\text{Cu}^+$ redox cycle is completed via the following reactions.



In addition to the above reactions, under the experimental conditions for the trimetal catalyst, i.e., $c(\text{H}_2\text{O}_2) = 20 \text{ mM}$, $c(\text{BPA}_{\text{ads}}) \cong 4.3 \mu\text{M}$, $c(\text{Cu}^{2+}) \cong 6.2 \mu\text{M}$, we can reasonably assume $\text{Cu}(\text{II})$, at least in part, forms complexes with BPA, preferentially on the OH group via σ bonding (Eq. 10) [53,54]. These are then susceptible to H_2O_2 attack (Eq. 11).



These reactions show that changing the local pH around the Cu active sites by visible light illumination changes the complexation behavior of BPA and disfavors the completion of the $\text{Cu}^{2+}/\text{Cu}^+$ cycle (Eq. 8 and 11). Although these reactions are recognised as not being the rate limiting steps they may explain the slower BPA kinetics with visible light turned on, and are corroborated with pH dependence behavior of the both catalysts. Note that a slightly higher overall degradation was observed in the illuminated experiments (82%—84%, and 82%—87% for ExC and C sample, respectively). Thus, in the long run, illumination still could provide a viable step for better longevity of the

catalysts.

Stability was evaluated first by monitoring the possible leached Mn, Fe and Cu species from the catalysts during the degradation processes using inductively coupled plasma technique. The concentration of Cu in aqueous solution (0.83 mg/L) is lower than the maximum allowed value 2 mg/L [55]. Iron, due to its encapsulation in the core of the particles, is not leached in measurable amounts in the solution. On the contrary, the leached amounts of Mn still exceeded their legal limits in drinking water (0.4 mg/L). [22,23] However, in the recycling experiments (see below) Mn is leached only during the initial degradation cycle ($<150 \text{ min}$, $\gamma = 1.39 \text{ mg/L}$) but practically ceases to be leached in the following hours of operation even after fresh spikes of BPA solution. Cu concentration, on the other hand, was higher after the first test than after continuous operation for 390 min. Also here, this implies that the majority of loosely coordinated Cu is leached during the first run of the photo-Fenton cycle.

3.3. Reusability tests

The reusability of the catalyst CuMnFeMS-ExC was tested in CSTR mode with consecutive spiking of suspension with fresh additions of BPA. For these tests, a lower concentration of BPA was chosen (5 mg/L) which was also the targeted concentration after spiking. The initial tests confirmed that degradation was complete within 150 min (Fig. 8, blue symbols). Therefore, this time was chosen as the start time for the next reuse test, without dark pre-equilibration applied. The trend shows that the catalyst is capable of continuous degradation of BPA within 3 cycles (Fig. 8, purple symbols). There was a decrease in degradation efficiency with consecutive cycles and degradation kinetics. However, the catalyst remained active even after 3 cycles of continuous usage. Leaching experiments showed that leaching of Fe was practically null, while the majority of Mn and Cu leaching occurred in the first cycle which explains the relatively good stability of the catalyst. Similar amorphous silica catalysts without the presence of Fe were shown to have worse long-term stability for degradation of dyes [13], hence this report presents an improvement in the catalyst design for practical applications.

Measurements of total organic carbon (TOC) content from samples at the end of their catalytic cycle (Table 4) showed the relative TOC concentrations to be 92% and 79% of the initial BPA TOC for sample CuMnFeMS-ExC taken after one and three cycles of photo-Fenton-like reaction, respectively. These results indicate that the catalyst is degrading the initial BPA solution to its degradation products and does

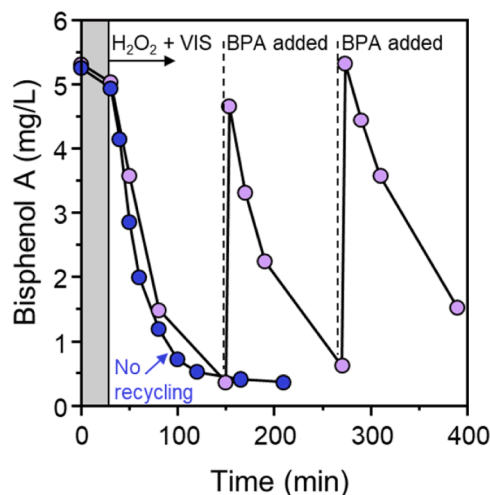


Fig. 8. Continuous use of catalyst CuMnFeMS-ExC under photo-Fenton conditions. Catalyst was not taken out of the reactor or regenerated during the whole continuous use test. Reaction conditions: $\gamma(\text{cat}) = 400 \text{ mg/L}$, $c(\text{H}_2\text{O}_2)_0 = 20 \text{ mM}$, $\gamma(\text{BPA}) = 5 \text{ mg/L}$, $\text{pH} = 5.7$ and VIS illumination applied.

Table 4

Concentrations of leached elements at the end of the corresponding reaction cycles for the extracted-calcined three-metal catalyst, as obtained by ICP-OES.

Catalyst	Cu (mg/L)	Mn (mg/L)	Fe (mg/L)	TOC (mg/L C)
CuMnFeMS-ExC (1st cycle)	0.83	1.31	< 0.1	4.75
CuMnFeMS-ExC (3rd cycle)	0.38	1.39	< 0.1	4.07

not fully oxidize the compound. However, after three cycles of reaction (upon the addition of three times the initial load of BPA) the TOC was still relatively low, thus confirming the long-lasting degradation capacity of the tri-metal catalyst.

4. Conclusions

Trimetallic Cu-Mn-Fe silica supported catalysts were prepared via direct synthesis by incorporating magnetic Fe₃O₄ nanoparticles and active catalytic/photocatalytic species (Cu and Mn) during the formation of the silica nanoparticles with interparticle mesoporosity.

The characterization results obtained by advanced microscopic and spectroscopic techniques revealed the presence of iron oxides with magnetic properties, incorporated manganese cations/oxo species into silica framework and CuO particles attached to the silica framework, which had two sizes: smaller (<5 nm, CuO_x) in the extracted sample - CuMnFeMS-ExC and larger (~25 nm, CuO) in the calcined sample - CuMnFeMS-C. This comprehensive characterization was confirmed and complemented by Mn, Fe and Cu K-edge XANES (X-ray absorption near edge structure) analysis to quantify the valence state and local symmetry of all three metal sites. Copper in CuMnFeMS-ExC is entirely in the form of small CuO nanoparticles (size of 2 nm), while in CuMnFeMS-C, 48% of Cu is in the form of crystalline (bulk) CuO and the rest (52%) is in the form of larger (10 nm) nanoparticles. In the case of Mn, 92% and 80% of the cations is in the form of incorporated Mn cations/oxospecies, for the CuMnFeMS-ExC and CuMnFeMS-C catalysts, respectively. The Fe cations are mainly in the 3+ valence state but occupy different ratios of tetrahedral and octahedral sites, leading to the 3-times higher magnetic properties of the calcined catalyst compared to the ExC.

The investigated solids were found to be efficient concerning the homolytic cleavage of H₂O₂ to hydroxyl radicals, with a further positive effect of hydroxyl radical formation observed under visible-light illumination thus acting as visible light active catalysts.

BPA degradation with the sample with smaller CuO particles had an optimal pH of 5.7, which was one unit lower than that of the sample with larger CuO species. In such a system, Mn and Cu species were responsible for both Fenton-like and photo-Fenton-like reactions, with the larger CuO particles performing better in the photo-Fenton-like reactions. However, when all three metals were combined, the extracted sample showed faster kinetics for BPA degradation, regardless of visible-light irradiation. This sample was able to continuously degrade the BPA solution over multiple runs with no apparent leaching of any of the metals after the first two hours of the reaction.

Understanding the structure-property-activity relationship of the designed multicomponent photocatalysts on a silica support with interparticle mesoporosity is extremely important not only for the rational design of the catalyst/photocatalyst for the described targeted water purification application, but also for other applications in photocatalysis, green chemistry and electrocatalysis.

CRedit authorship contribution statement

Andraž Šuligoj: Investigation, Methodology, Formal analysis, Writing – original draft. **Ivalina Trendafilova:** Investigation, Methodology, Formal analysis, Writing – original draft. **Ksenija Maver:** Formal analysis, Writing – original draft. **Albin Pintar:** Formal analysis, Writing – original draft, Writing – review & editing, Funding acquisition. **Alenka**

Ristić: Formal analysis, Writing – original draft. **Goran Dražić:** Formal analysis, Writing – original draft. **Wael H.M. Abdelraheem:** Formal analysis, Writing – original draft. **Zvonko Jagličić:** Formal analysis, Writing – original draft. **Iztok Arčon:** Synchrotron measurements, Writing – review & editing, Funding acquisition. **Nataša Zabukovec Logar:** Writing – review & editing, Funding acquisition. **Dionysios D. Dionysiou:** Writing – review & editing, Funding acquisition. **Nataša Novak Tušar:** Conceptualization, Supervision, Writing – review & editing, Project administration, Funding acquisition.

Declaration of Competing Interest

The authors declare that they have no known competing financial interests or personal relationships that could have appeared to influence the work reported in this paper.

Data Availability

Data will be made available on request.

Acknowledgements

This research work was supported by the Slovenian Research and Innovation Agency (research programs P1-0021, P1-0134, P1-0418 and P2-0150, and Slovenia-USA Research Bilateral Project BI-US/18-19-039). The SEM and nitrogen physisorption measurements were done by Mojca Opresnik and the XRD measurements by Edi Kranjc, both from the National Institute of Chemistry, Ljubljana, for that we are very grateful. D. D. Dionysiou also acknowledges support from the University of Cincinnati through the Herman Schneider Professorship in the College of Engineering and Applied Sciences. Access to ESRF synchrotron radiation facility (beamline BM23, project MA-5036) is acknowledged. Kirill Lomachenko and Cesare Atzori are acknowledged for expert advice on beamline operation.

Appendix A. Supporting information

Supplementary data associated with this article can be found in the online version at [doi:10.1016/j.jece.2023.110369](https://doi.org/10.1016/j.jece.2023.110369).

References

- [1] Nanocatalysts and other nanomaterials for water remediation from organic pollutants, in: F. Lu, D. Astruc (Eds.), *Coord. Chem. Rev.*, 408, 2020, <https://doi.org/10.1016/j.ccr.2020.213180>.
- [2] Y. Xu, T. Liu, Y. Zhang, F. Ge, R.M. Steel, L. Sun, *Advances in technologies for pharmaceuticals and personal care products removal*, *J. Mater. Chem. A* 5 (2017) 12001–12014, <https://doi.org/10.1039/C7TA03698A>.
- [3] N. Wang, T. Zheng, G. Zhang, P. Wang, *A review on Fenton-like processes for organic wastewater treatment*, *J. Environ. Chem. Eng.* 4 (2016) 762–787, <https://doi.org/10.1016/j.jece.2015.12.016>.
- [4] D. Hasan, A.A. Abdul Raman, W. Daud, *On the limitation of fenton oxidation operational parameters: a review*, *Int. J. Chem. React. Eng.* 10 (2012), <https://doi.org/10.1515/1542-6580.2913>.
- [5] L. Clarizia, D. Russo, I. Di Somma, R. Marotta, R. Andreozzi, *Homogeneous photo-Fenton processes at near neutral pH: a review*, *Appl. Catal. B Environ.* 209 (2017) 358–371, <https://doi.org/10.1016/j.apcatb.2017.03.011>.
- [6] J. Rodríguez-Chueca, J. Carbajo, P. García-Muñoz, *Intensification of photo-assisted advanced oxidation processes for water treatment: a critical review*, *Catalysts* 13 (2023) 401, <https://doi.org/10.3390/catal13020401>.
- [7] N. Thomas, D.D. Dionysiou, S.C. Pillai, *Heterogeneous Fenton catalysts: a review of recent advances*, *J. Hazard. Mater.* 404 (2021), 124082, <https://doi.org/10.1016/j.jhazmat.2020.124082>.
- [8] Y. Zhu, R. Zhu, Y. Xi, J. Zhu, G. Zhu, H. He, *Strategies for enhancing the heterogeneous Fenton catalytic reactivity: a review*, *Appl. Catal. B Environ.* 255 (2019), 117739, <https://doi.org/10.1016/j.apcatb.2019.05.041>.
- [9] A.D. Bokare, W. Choi, *Review of iron-free Fenton-like systems for activating H₂O₂ in advanced oxidation processes*, *J. Hazard. Mater.* 275 (2014) 121–135, <https://doi.org/10.1016/j.jhazmat.2014.04.054>.
- [10] S. Hussain, E. Aneggi, D. Goi, *Catalytic activity of metals in heterogeneous Fenton-like oxidation of wastewater contaminants: a review*, *Environ. Chem. Lett.* 19 (2021) 2405–2424, <https://doi.org/10.1007/s10311-021-01185-z>.

- [11] E.J. Kim, D. Oh, C.S. Lee, J. Gong, J. Kim, Y.S. Chang, Manganese oxide nanorods as a robust Fenton-like catalyst at neutral pH: Crystal phase-dependent behavior, *Catal. Today* 282 (2017) 71–76, <https://doi.org/10.1016/j.cattod.2016.03.034>.
- [12] N.N. Tušar, D. Maučec, M. Rangus, I. Arčon, M. Mazaj, M. Cotman, A. Pintar, V. Kaučič, Manganese functionalized silicate nanoparticles as a Fenton-type catalyst for water purification by advanced oxidation processes (AOP), *Adv. Funct. Mater.* 22 (2012) 820–826, <https://doi.org/10.1002/adfm.2011102361>.
- [13] A. Šuligoj, A. Ristić, G. Dražić, A. Pintar, N.Z. Logar, N.N. Tušar, Bimetal Cu-Mn porous silica-supported catalyst for Fenton-like degradation of organic dyes in wastewater at neutral pH, *Catal. Today* 358 (2020) 270–277, <https://doi.org/10.1016/j.cattod.2020.03.047>.
- [14] L. Lyu, L. Zhang, C. Hu, Enhanced Fenton-like degradation of pharmaceuticals over framework copper species in copper-doped mesoporous silica microspheres, *Chem. Eng. J.* 274 (2015) 298–306, <https://doi.org/10.1016/j.cej.2015.03.137>.
- [15] T. Khudkham, D. Channei, B. Pinchaipat, R. Chotima, Degradation of methylene blue with a Cu(II)-quinoline complex immobilized on a silica support as a photo-fenton-like catalyst, *ACS Omega* 7 (2022) 33258–33265, <https://doi.org/10.1021/acsomega.2c03770>.
- [16] A. Grau-Atienza, E. Serrano, N. Linares, P. Svedlindh, G. Seisenbaeva, J. García-Martínez, Magnetically separable mesoporous Fe₃O₄/silica catalysts with very low Fe₃O₄ content, *J. Solid State Chem.* 237 (2016) 138–143, <https://doi.org/10.1016/j.jssc.2015.12.026>.
- [17] I.A. Barbosa, P.C. de Sousa Filho, D.L. da Silva, F.B. Zanardi, L.D. Zanatta, A.J.A. de Oliveira, O.A. Serra, Y. Iamamoto, Metallophyrins immobilized in Fe₃O₄@SiO₂ mesoporous microspheres: Reusable biomimetic catalysts for hydrocarbon oxidation, *J. Colloid Interface Sci.* 469 (2016) 296–309, <https://doi.org/10.1016/j.jcis.2016.01.059>.
- [18] M. Abdollahi-Alibeik, A. Rezaei-poor-Anari, Fe₃O₄@B-MCM-41: A new magnetically recoverable nanostructured catalyst for the synthesis of polyhydroquinolines, *J. Magn. Mater.* 398 (2016) 205–214, <https://doi.org/10.1016/j.jmmm.2015.09.048>.
- [19] A.S. Teja, P.-Y. Koh, Synthesis, properties, and applications of magnetic iron oxide nanoparticles, *Prog. Cryst. Growth Charact. Mater.* 55 (2009) 22–45, <https://doi.org/10.1016/j.pcrysgrow.2008.08.003>.
- [20] M.C. Mascolo, Y. Pei, T.A. Ring, Room temperature co-precipitation synthesis of magnetite nanoparticles in a Large pH window with different bases, *Materials* 6 (2013) 5549–5567, <https://doi.org/10.3390/ma6125549>.
- [21] S. Brunauer, P.H. Emmett, E. Teller, Adsorption of gases in multimolecular layers, *J. Am. Chem. Soc.* 60 (1938) 309–319, <https://doi.org/10.1021/ja01269a023>.
- [22] T.A. Zepeda, J.L.G. Fierro, B. Pawelec, R. Nava, T. Klimova, G.A. Fuentes, T. Halachev, Synthesis and characterization of Ti-HMS and CoMo/Ti-HMS oxide materials with varying Ti content, *Chem. Mater.* 17 (2005) 4062–4073, <https://doi.org/10.1021/cm0500051>.
- [23] E.P. Barrett, L.G. Joyner, P.P. Halenda, The determination of pore volume and area distributions in porous substances. I. Computations from nitrogen isotherms, *J. Am. Chem. Soc.* 73 (1951) 373–380, <https://doi.org/10.1021/ja011145a126>.
- [24] B. Ravel, M. Newville, ATHENA, ARTEMIS, HEPHAESTUS: data analysis for X-ray absorption spectroscopy using IFEFFIT, *J. Synchrotron Radiat.* 12 (2005) 537–541, <https://doi.org/10.1107/S0909049505012719>.
- [25] R.L. ReboDOS, P.J. Vikesland, Effects of oxidation on the magnetization of nanoparticulate magnetite, *Langmuir* 26 (2010) 16745–16753, <https://doi.org/10.1021/la102461z>.
- [26] M. Popova, I. Trendafilova, Á. Szegedi, D. Momekova, J. Mihály, G. Momekov, L.F. L.F. Kiss, K. Lázár, N. Koseva, Novel SO₃H functionalized magnetic nanoporous silica/polymer nanocomposite as a carrier in a dual-drug delivery system for anticancer therapy, *Microporous Mesoporous Mater.* 263 (2018) 96–105, <https://doi.org/10.1016/j.micromeso.2017.12.005>.
- [27] P.A. van Aken, B. Liebscher, Quantification of ferrous/ferric ratios in minerals: new evaluation schemes of Fe L₂₃ electron energy-loss near-edge spectra, *Phys. Chem. Miner.* 29 (2002) 188–200, <https://doi.org/10.1007/s00269-001-0222-6>.
- [28] R. Vigliaturo, S. Pollastri, R. Gieré, A.F. Gualtieri, G. Dražić, Experimental quantification of the Fe-valence state at amosite-asbestos boundaries using acSTEM dual-electron energy-loss spectroscopy, *Am. Miner.* 104 (2019) 1820–1828, <https://doi.org/10.2138/am-2019-7218>.
- [29] M. Testa-Anta, M.A. Ramos-Docampo, M. Comesaña-Hermo, B. Rivas-Murias, V. Salgueiriño, Raman spectroscopy to unravel the magnetic properties of iron oxide nanocrystals for bio-related applications, *Nanoscale Adv.* 1 (2019) 2086–2103, <https://doi.org/10.1039/c9na00064j>.
- [30] I. Chamritski, G. Burns, Infrared- and raman-active phonons of magnetite, maghemite, and hematite: a computer simulation and spectroscopic study, *J. Phys. Chem. B* 109 (2005) 4965–4968, <https://doi.org/10.1021/jp048748h>.
- [31] C.S.S.R. Kumar, Raman Spectroscopy for Nanomaterials Characterization, Springer Berlin Heidelberg, Berlin, Heidelberg, 2012, <https://doi.org/10.1007/978-3-642-20620-7>.
- [32] T. Jiang, A.S. Poyraz, A. Iyer, Y. Zhang, Z. Luo, W. Zhong, R. Miao, A.M. El-Sawy, C.J. Guild, Y. Sun, D.A. Kriz, S.L. Suib, Synthesis of mesoporous iron oxides by an inverse micelle method and their application in the degradation of orange ii under visible light at neutral pH, *J. Phys. Chem. C* 119 (2015) 10454–10468, <https://doi.org/10.1021/acs.jpcc.5b02057>.
- [33] K. Tadzysak, A. Kertmen, E. Coy, R. Andruszkiewicz, S. Jurga, K. Chybczyn, Journal of Magnetism and Magnetic Materials Spectroscopic and magnetic studies of highly dispersible superparamagnetic silica coated magnetite nanoparticles, 433 (2017) 254–261, <https://doi.org/10.1016/j.jmmm.2017.03.025>.
- [34] W. Wu, C.Z. Jiang, V.A.L. Roy, Designed synthesis and surface engineering strategies of magnetic iron oxide nanoparticles for biomedical applications, *Nanoscale* 8 (2016) 19421–19474, <https://doi.org/10.1039/C6NR07542H>.
- [35] L. Machala, J. Tuček, R. Zbořil, Polymorphous transformations of nanometric iron (III) oxide: a review, *Chem. Mater.* 23 (2011) 3255–3272, <https://doi.org/10.1021/cm200397g>.
- [36] S.L. Nauer, A.S. Rosen, H. Kim, R.Q. Snurr, P.C. Stair, J.M. Notestein, Evidence for copper dimers in low-loaded Cu₂O/SiO₂ catalysts for cyclohexane oxidative dehydrogenation, *ACS Catal.* 8 (2018) 9775–9789, <https://doi.org/10.1021/acscatal.8b02532>.
- [37] Y. Deng, A.D. Handoko, Y. Du, S. Xi, B.S. Yeo, In situ raman spectroscopy of copper and copper oxide surfaces during electrochemical oxygen evolution reaction: identification of Cu III oxides as catalytically active species, *ACS Catal.* 6 (2016) 2473–2481, <https://doi.org/10.1021/acscatal.6b00205>.
- [38] C.M. Julien, M. Massot, C. Poinsignon, Lattice vibrations of manganese oxides: Part I. Periodic structures, *Spectrochim. Acta - Part A Mol. Biomol. Spectrosc.* 60 (2004) 689–700, [https://doi.org/10.1016/S1386-1425\(03\)00279-8](https://doi.org/10.1016/S1386-1425(03)00279-8).
- [39] T. Žumbar, A. Ristić, G. Dražić, H. Lazarova, J. Volavšek, A. Pintar, N. Zabukovec Logar, N.N. Tušar, Influence of alumina precursor properties on Cu-Fe alumina supported catalysts for total toluene oxidation as a model volatile organic air pollutant, *Catalysts* 11 (2021) 252, <https://doi.org/10.3390/catal11020252>.
- [40] M. Wahiduzzaman, S. Wang, J. Schnee, A. Vimont, V. Ortiz, P.G. Yot, R. Retoux, M. Daturi, J.S. Lee, J.S. Chang, C. Serre, G. Maurin, S. Devautour-Vinot, A. High, Proton conductive hydrogen-sulfate decorated titanium carboxylate metal-organic framework, *ACS Sustain. Chem. Eng.* 7 (2019) 5776–5783, <https://doi.org/10.1021/acssuschemeng.8b05306>.
- [41] J. Perez-Ramirez, M. Santhosh Kumar, A. Brückner, Reduction of N₂O with CO over FeMFI zeolites: influence of the preparation method on the iron species and catalytic behavior, *J. Catal.* 223 (2004) 13–27, <https://doi.org/10.1016/j.jcat.2004.01.007>.
- [42] A. Ristić, M. Mazaj, I. Arčon, N. Daneu, N. Zabukovec Logar, R. Gläser, N.N. Tušar, New insights into manganese local environment in MnS-1 nanocrystals, *Cryst. Growth Des.* 19 (2019) 3130–3138, <https://doi.org/10.1021/acs.cgd.8b01181>.
- [43] Y. Meng, H.C. Genuino, C.-H. Kuo, H. Huang, S.-Y. Chen, L. Zhang, A. Rossi, S. L. Suib, One-step hydrothermal synthesis of manganese-containing MFI-Type Zeolite, Mn-ZSM-5, characterization, and catalytic oxidation of hydrocarbons, *J. Am. Chem. Soc.* 135 (2013) 8594–8605, <https://doi.org/10.1021/ja4013936>.
- [44] I. Trendafilova, A. Šuligoj, A. Ristić, N. Van de Velde, G. Dražić, M. Oprešnik, N. Zabukovec Logar, A. Pintar, N. Novak Tušar, Evolution of surface catalytic sites on bimetallic silica-based Fenton-like catalysts for degradation of dyes with different molecular charges, *Nanomaterials* 10 (2020) 2419, <https://doi.org/10.3390/nano10122419>.
- [45] Y. Guo, Y. Zhao, S. Wang, C. Jiang, J. Zhang, Relationship between the zeta potential and the chemical agglomeration efficiency of fine particles in flue gas during coal combustion, *Fuel* 215 (2018) 756–765, <https://doi.org/10.1016/j.fuel.2017.11.005>.
- [46] M. Zabilskiy, I. Arčon, P. Djinović, E. Tchernychova, A. Pintar, In-situ XAS study of catalytic N₂O decomposition over CuO/CeO₂ catalysts, *ChemCatChem* 13 (2021) 1814–1823, <https://doi.org/10.1002/cctc.202001829>.
- [47] M.-H. Phan, J. Alonso, H. Khurshid, P. Lampen-Kelley, S. Chandra, K. Stojak Repa, Z. Nemati, R. Das, Ó. Iglesias, H. Srikanth, Exchange bias effects in iron oxide-based nanoparticle systems, *Nanomaterials* 6 (2016) 221, <https://doi.org/10.3390/nano6110221>.
- [48] I. Arčon, J. Kolar, A. Kodre, D. Hanzel, M. Strlič, XANES analysis of Fe valence in iron gall inks, *X-Ray Spectrom.* 36 (2007) 199–205, <https://doi.org/10.1002/xrs.962>.
- [49] R. Dominko, C. Sirisopanaporn, C. Masquelier, D. Hanzel, I. Arčon, M. Gabersček, I. Arcon, M. Gabersček, On the origin of the electrochemical capacity of Li₂Fe_{0.8}Mn_{0.2}SiO₄, *J. Electrochem. Soc.* 157 (2010) A1309, <https://doi.org/10.1149/1.3491368>.
- [50] M.P. Pachamuthu, S. Karthikeyan, R. Maheswari, A.F. Lee, A. Ramanathan, Fenton-like degradation of Bisphenol A catalyzed by mesoporous Cu/TUD-1, *Appl. Surf. Sci.* 393 (2017) 67–73, <https://doi.org/10.1016/j.apsusc.2016.09.162>.
- [51] X. Zhang, J. Wang, B. Xiao, Y. Pu, Y. Yang, J. Geng, D. Wang, X. Chen, Y. Wei, K. Xiong, Y. Zhu, Resin-based photo-self-Fenton system with intensive mineralization by the synergistic effect of holes and hydroxyl radicals, *Appl. Catal. B Environ.* 315 (2022), 121525, <https://doi.org/10.1016/j.apcatb.2022.121525>.
- [52] G. Žerjav, A. Albreht, I. Vovk, A. Pintar, Revisiting terephthalic acid and coumarin as probes for photoluminescent determination of hydroxyl radical formation rate in heterogeneous photocatalysis, *Appl. Catal. A Gen.* 598 (2020), 117566, <https://doi.org/10.1016/j.apcata.2020.117566>.
- [53] J.Y. Park, B.C. Lee, J.S. Ra, J. Lee, S.D. Kim, Effect of copper complexation on the estrogenic activities of endocrine-disrupting compounds using E-screen bioassay, *Environ. Toxicol. Chem.* 27 (2008) 535, <https://doi.org/10.1897/07-316.1>.
- [54] S. Liang, J. Han, Z. Yuxuan, W. Jun, L. Lingling, W. Lingyun, Z. Yang, Facile synthesis of copper-based bimetallic oxides for efficient removal of bisphenol a via Fenton-like degradation, *Sep. Purif. Technol.* 279 (2021), 119724, <https://doi.org/10.1016/j.seppur.2021.119724>.
- [55] European Commission, Directive 2000/60/EC of the European Parliament and of the Council of 23 October 2000 establishing a framework for Community action in the field of water policy, *J. Eur. Parliam.* L327 (2000).